

CFD simulation of compressible two-phase sloshing flow in a LNG tank

Hamn-Ching Chen*

Ocean Engineering Program, Zachry Department of Civil Engineering, Texas A & M University, USA
(Received January 4, 2011, Accepted February 11, 2011)

Abstract. Impact pressure due to sloshing is of great concern for the ship owners, designers and builders of the LNG carriers regarding the safety of LNG containment system and hull structure. Sloshing of LNG in partially filled tank has been an active area of research with numerous experimental and numerical investigations over the past decade. In order to accurately predict the sloshing impact load, a new numerical method was developed for accurate resolution of violent sloshing flow inside a three-dimensional LNG tank including wave breaking, jet formation, gas entrapping and liquid-gas interaction. The sloshing flow inside a membrane-type LNG tank is simulated numerically using the Finite-Analytic Navier-Stokes (FANS) method. The governing equations for two-phase air and water flows are formulated in curvilinear coordinate system and discretized using the finite-analytic method on a non-staggered grid. Simulations were performed for LNG tank in transverse and longitudinal motions including horizontal, vertical, and rotational motions. The predicted impact pressures were compared with the corresponding experimental data. The validation results clearly illustrate the capability of the present two-phase FANS method for accurate prediction of impact pressure in sloshing LNG tank including violent free surface motion, three-dimensional instability and air trapping effects.

Keywords: LNG tank sloshing; compressible two-phase flow; computational fluid dynamics; Navier-Stokes equations; level-set function; impact pressure.

1. Introduction

Due to the growing LNG market, there is a strong demand of new LNG carriers with significantly larger cargo capacity. The safety of the new LNG liquid cargo hold and containment system for the membrane-type LNG carriers with a wide range of filling levels has to be re-evaluated. Sloshing model tests have been performed by, among others, Faltinsen *et al.* (2000), Lee *et al.* (2005b), Hwang (2006), Lee *et al.* (2006a) and Lee *et al.* (2006b) to simulate six degrees of freedom ship motions and determine the critical sloshing load. In these experiments, the Froude scaling law is adopted to scale down the geometry, tank motion, and gravitational effects. Impact pressures obtained from the model tests are then scaled up to prototype using the Euler scaling with the full-scale pressure proportional to the liquid density and length dimensions. The model test is considered to be the most reliable method in predicting the maximum impact pressure especially for violent sloshing. However, the true impact load in the full scale LNG tank is still unknown due to the scale effects associated with other unmatched parameters such as fluid viscosity, gas/liquid density ratio,

*Corresponding author, E-mail: hcchen@civil.tamu.edu

gas compressibility, ullage pressure, and wall elasticity.

Numerical simulations have also been used extensively for the simulation of sloshing flow in LNG tank. Considering the sloshing flows as free surfaces flows, there are two major approaches, namely interface-tracking and interface-capturing methods, to find the shape of the free surface. Because of complexity of the free surface phenomena in sloshing, the interface-capturing method is more often used for sloshing flow simulations. The interface-capturing method can be categorized into three different approaches, Marker and Cell (MAC), Volume of Fluid (VOF) and Level Set Method. The smoothed particle hydrodynamics (SPH) method which is developed from MAC is used by Iglesias *et al.* (2004) and Nam and Kim (2006) for simulating violent sloshing flows in two-dimensional tanks. Kim (2001, 2004) used the SOLA-SURF to solve the sloshing problem in rectangular and prismatic tanks. Lee *et al.* (2005a) employed a commercial code FLOW3D with VOF method for the free surface flow simulation for parametric sensitivity study on LNG tank sloshing load. Loots *et al.* (2004) presented an improved VOF (iVOF) method to account for mass conservation in cut cells and eliminate numerical spikes in pressure signals for sloshing tank simulation. Wemmenhove *et al.* (2007, 2009) extended iVOF to incorporate a compressible two-phase flow model for more accurate simulation of LNG tank sloshing. Guilcher *et al.* (2010) employed a two-phase SPH model for the simulation of liquid impacts including entrapped gas. Chen *et al.* (2009) developed a compressible two-fluid flow model for the simulation of liquid sloshing in 2D LNG tanks. Cao *et al.* (2010) performed a comparative study of sloshing load in a rectangular tank using linear and nonlinear potential flow models and three CFD codes (SPH, FEFLO and OpenFOAM), Peric *et al.* (2007) performed coupled simulation of a floating vessel with two internal LNG tanks using the STAR-software.

In the present study, we employ the level-set Reynolds-Averaged Navier-Stokes (RANS) method of Chen and Yu (2006, 2009), Yu *et al.* (2007) and Chen (2010) for time-domain simulation of sloshing in a three-dimensional membrane-type LNG tank. The present interface-capturing method was developed based on the level set method of Osher and Sethian (1988). In the level set formulation, the level set function ϕ is typically defined as a signed distance from the interface; $\phi < 0$ in air region, $\phi > 0$ in liquid region, and $\phi = 0$ on the air-liquid interface. The value of ϕ is initialized by the physical distance from the interface. Then it is advected by the local velocity field using the advection equation

$$\frac{\partial \phi}{\partial t} + \vec{V} \cdot \nabla \phi = 0 \quad (1)$$

The interface can be identified at any time by locating the zero level set. However, the computed ϕ may not remain the signed distance from the interface after several numerical iterations. It is necessary to perform the following redistancing process for every time step

$$\frac{\partial \phi}{\partial \tau} = \text{sign}(\phi_0) \cdot (1 - |\nabla \phi|) \quad (2)$$

This equation guarantees that ϕ has the same sign and zero level set as ϕ_0 and satisfies the condition that $|\nabla \phi| = 1$. The level set method was shown to lower the difficulties in handling topological merging for violent free surface motion problems. More details of the level set methods can be found in Sethian (1996).

In the present study, the level set method has been incorporated into the chimera RANS method of Chen and Chen (1998) for the prediction of sloshing impact load on membrane-type LNG tanks.

The governing equations are formulated in curvilinear coordinate system and discretized using the finite-analytic method of Chen *et al.* (1990) on a non-staggered grid. For the additional level set equations of evolution and re-initialization, we use the 3rd-order TVD (total variation diminishing) Runge-Kutta scheme (Yue *et al.* 2003) for time derivative, and the 3rd-order ENO (essentially non-oscillatory) scheme for spatial derivatives. The present interface-capturing method was validated in earlier in Chen and Yu (2006, 2009) for several benchmark cases including a stationary circle, the Zalesak's problem, the stretching of a circular fluid element under prescribed free motion, and a high-speed ship undergoing heave and pitch motions in regular waves. The level set method was then incorporated into the chimera RANS method of Chen and Chen (1998) for complex free surface flow simulations. Calculations were performed for both the two-dimensional and three-dimensional membrane-type LNG tank under prescribed transverse and longitudinal sloshing motions. The simulation results clearly demonstrated the capability of the level-set FANS method for accurate prediction of violent free surface flows and the associated impact load induced by the sloshing motion of LNG tanks.

2. Theoretical formulation

In the present compressible two-phase flow formulation, both the density and viscosity at the air-water interfaces depend on the level set function. The fluid properties are assumed to vary smoothly across a narrow transition zone around the free surface. This enables us to obtain accurate and stable numerical results for violent free surface motions induced by the sloshing flow in LNG tanks.

In the present algorithm, the interface is the zero level set of ϕ

$$\Gamma = \{\vec{x} | \phi(\vec{x}, t) = 0\} \quad (3)$$

By defining $\phi < 0$ for air region and $\phi > 0$ for water region, we have

$$\phi(\vec{x}, t) \begin{cases} > 0 & \text{if } \vec{x} \in \text{water} \\ = 0 & \text{if } \vec{x} \in \Gamma \\ < 0 & \text{if } \vec{x} \in \text{air} \end{cases} \quad (4)$$

The evolution of ϕ is given by the advection eq. (1) in the transition zone defined by $|\phi| \leq \varepsilon$, where ε is the half thickness of the interface. In the transition zone, the fluid properties are smoothed by Heaviside function

$$H(\phi) = \begin{cases} 0 & \text{if } \phi < -\varepsilon \\ \frac{1}{2} \left(1 + \frac{\phi}{\varepsilon} + \frac{1}{\pi} \sin\left(\frac{\pi\phi}{\varepsilon}\right) \right) & \text{if } -\varepsilon \leq \phi \leq \varepsilon \\ 1 & \text{if } \phi > \varepsilon \end{cases} \quad (5)$$

More specifically, the density and viscosity are calculated in the following way

$$\begin{aligned}\rho(\phi) &= \rho_a + (\rho_w - \rho_a) \cdot H(\phi) \\ \mu(\phi) &= \mu_a + (\mu_w - \mu_a) \cdot H(\phi)\end{aligned}\quad (6)$$

where the subscripts ‘a’ and ‘w’ represent air and water, respectively.

After a new level set value ϕ_0 is obtained in each time step, it is necessary to solve the re-distancing eq. (2) in order to ensure that the level set value remains as a real distance. However, it is well known that numerical errors may accumulate due to repeated re-distance operations on a level set function. In order to prevent the straying of the zero level set from initial position even after many iterations, a mass constraint term proposed by Sussman and Fatemi (1999) is added to eq. (2) as follows

$$\frac{\partial \phi}{\partial \tau} = L(\phi_0, \phi) + \lambda_{ij} f(\phi) \quad (7)$$

where

$$L(\phi_0, \phi) = \text{sign}(\phi_0)(1 - |\nabla \phi|); f(\phi) \equiv H'(\phi)|\nabla \phi| \quad (8)$$

The coefficient λ is determined by

$$\lambda_{ij} = \frac{-\int_{\Omega_{ij}} H'(\phi) L(\phi_0, \phi)}{\int_{\Omega_{ij}} H'(\phi) f(\phi)} \quad (9)$$

for every grid cell $\Omega_{ij} = \{(x, y) | x_{i-1/2} < x < x_{i+1/2} \text{ and } y_{j-1/2} < y < y_{j+1/2}\}$. A more detailed description of the mass constraint term is given in Sussman and Fatemi (1999).

In the present study, the air is treated as compressible flow and governed by the continuity, momentum (i.e., Navier-Stokes) and energy equations:

$$\frac{\partial \rho}{\partial t} + v^m \rho_{,m} = 0 \quad (10)$$

$$\rho \left(\frac{\partial v^i}{\partial t} + v^m v^i_{,m} \right) = \rho f^i - g^{im} p_{,m} + (\lambda + \mu) g^{ij} v^m_{,mj} + \mu g^{mn} v^i_{,mn} \quad (11)$$

$$\rho \left(\frac{\partial T}{\partial t} + v^m T_{,m} \right) = \kappa g^{mn} T_{,mn} + Q - p v^m_{,m} + \lambda v^m_{,m} + \mu (v^m_{,n} v^n_{,m} + g_{ij} g^{mn} v^i_{,m} v^j_{,n}) \quad (12)$$

where ρ , μ and λ are the density, viscosity, and second viscosity of the air, respectively. For the air considered here, the second viscosity is given by $\lambda = 2\mu/3$ and the equation of state $p = \rho RT$ is used to provide closure for (ρ, v^i, p, T) following the ideal gas law. In the present study, the air flow is assumed to be isothermal (i.e., $T = \text{constant}$). Under this condition, it is not necessary to solve the energy equation and the fluid density is linearly proportional to the absolute pressure of the air following the ideal gas law $p = \rho RT$.

For the air-water interface flow considered in the present sloshing simulations, the water

compressibility is negligible since the range of pressure variation in the tank is relatively small and the corresponding Mach number is very low. Therefore, the equation of state $p = \rho RT$ for ideal gas is not applicable for water and the density in eqs. (10)-(12) should be treated as constant. This implies that the water flow cannot be solved using the same set of equations for air and must be solved using the incompressible Navier-Stokes equations

$$v_{,m}^m = 0 \quad (14)$$

$$\rho_w \left(\frac{\partial v^i}{\partial t} + v^m v_{,m}^i \right) = \rho_w f^i - g^{im} p_{,m} + \mu g^{mn} v_{,mn}^i \quad (15)$$

3. Numerical method

In the present study, eq. (1) is transformed into general curvilinear coordinates $\xi^i = (\xi, \eta, \zeta)$ and advanced in time using the 3rd-order TVD Runge-Kutta scheme which is total variation stable (Yue *et al.* 2003)

$$\begin{cases} \phi^{(1)} = \phi^n - \Delta t \cdot R(\phi^n) \\ \phi^{(2)} = \frac{3}{4}\phi^{(n)} + \frac{1}{4}\phi^{(1)} - \frac{\Delta t}{4}R(\phi^{(1)}) \\ \phi^{(n+1)} = \frac{1}{3}\phi^{(n)} + \frac{2}{3}\phi^{(2)} - \frac{2\Delta t}{3}R(\phi^{(2)}) \end{cases} \quad (16)$$

where $R(\phi) = v^i \frac{\partial \phi}{\partial \xi^i}$ and the spatial operator. In Chen and Yu (2006, 2009), the spatial operator $R(\phi)$

was discretized using a 3rd-order Hamilton-Jacobi Essentially Non-oscillatory (HJ ENO) scheme. In the present study, a 5th-order accurate Hamilton-Jacobi Weighted Essentially Non-oscillatory (HJ WENO) scheme was adopted to further improve the accuracy of the spatial discretization for the level-set function

$$v^i \frac{\partial \phi}{\partial \xi^i} = \max(v^1, 0) \phi_{\xi}^- + \min(v^1, 0) \phi_{\xi}^+ + \max(v^2, 0) \phi_{\eta}^- + \min(v^2, 0) \phi_{\eta}^+ + \max(v^3, 0) \phi_{\zeta}^- + \min(v^3, 0) \phi_{\zeta}^+ \quad (17)$$

In the third-order accurate HJ ENO scheme, the spatial derivative $(\phi_{\xi}^-)_i$ is approximated by one of the following three upwind discretizations

$$\begin{cases} \phi_{\xi}^1 = \frac{2v_1 - 7v_2 + 11v_3}{6} \\ \phi_{\xi}^2 = \frac{-v_2 - 5v_3 + 2v_4}{6} \\ \phi_{\xi}^3 = \frac{2v_3 + 5v_4 - v_5}{6} \end{cases} \quad (18)$$

where $v_1 = D^- \phi_{i-2}$, $v_2 = D^- \phi_{i-1}$, $v_3 = D^- \phi_i$, $v_4 = D^- \phi_{i+1}$, $v_5 = D^- \phi_{i+2}$ and $D^- \phi_i = \phi_i - \phi_{i-1}$. The HJ ENO scheme choose the single approximation with the smallest error by selecting the smoothest possible polynomial interpolation of ϕ . Jiang and Shu (1996) and Jiang and Peng (2000) proposed a weighted ENO (WENO) method by choosing a convex combination of the above three ENO approximations in order to obtain the optimal 5th-order accuracy in the smooth region of the flow. Across a discontinuity or sharp gradient, however, the weights associated with the large gradient terms will be reduced to minimize its contribution and the resulting errors.

The HJ WENO approximation of $(\phi_\xi)_i$ is a convex combination given by

$$\phi_\xi = \omega_1 \phi_\xi^1 + \omega_2 \phi_\xi^2 + \omega_3 \phi_\xi^3 \quad (19)$$

where the weighting functions are defined as

$$\omega_1 = \frac{\alpha_1}{\alpha_1 + \alpha_2 + \alpha_3}, \quad \omega_2 = \frac{\alpha_2}{\alpha_1 + \alpha_2 + \alpha_3}, \quad \omega_3 = \frac{\alpha_3}{\alpha_1 + \alpha_2 + \alpha_3} \quad (20)$$

with

$$\alpha_1 = \frac{0.1}{(S_1 + \varepsilon)^2}, \quad \alpha_2 = \frac{0.6}{(S_2 + \varepsilon)^2}, \quad \alpha_3 = \frac{0.3}{(S_3 + \varepsilon)^2}$$

and (S_1, S_2, S_3) are the smoothness estimates given by

$$\begin{aligned} S_1 &= \frac{13}{12}(v_1 - 2v_2 + v_3)^2 + \frac{1}{4}(v_1 - 4v_2 + 3v_3)^2 \\ S_2 &= \frac{13}{12}(v_2 - 2v_3 + v_4)^2 + \frac{1}{4}(v_2 - v_4)^2 \\ S_3 &= \frac{13}{12}(v_3 - 2v_4 + v_5)^2 + \frac{1}{4}(3v_3 - 4v_4 + v_5)^2 \end{aligned}$$

A small value of $\varepsilon = 10^{-6}$ is chosen to avoid division by zero in the definition of α_k in the present study.

4. Geometry and motions

Fig. 1 shows the geometry of the LNG tank used in the present simulations. The dimension of the tank in full scale is 37.9 m \times 43.72 m \times 26.75 m, (tank breadth) \times (tank length) \times (tank height). The lower and upper chamfer angles (γ_b, γ_u) are both equal to 135°. The lower chamfer height h_l is 3.77 m, while the upper chamfer height h_u is 8.63 m. For all the computations, the filling level is specified in terms of d/h (%H).

Model tests were conducted by Lee *et al.* (2006b) on a 1/70 scale model with dimensions of 541.36 mm \times 624.50 mm \times 382.20 mm. The model was instrumented with 17 pressure gages to measure the impact pressure on the LNG tank walls. Fig. 2 shows the positions of all 17 sensors in the model test. The numbers in this figure are the distances in model scale. The sampling frequency of the pressure gages is about 20,000 Hz.

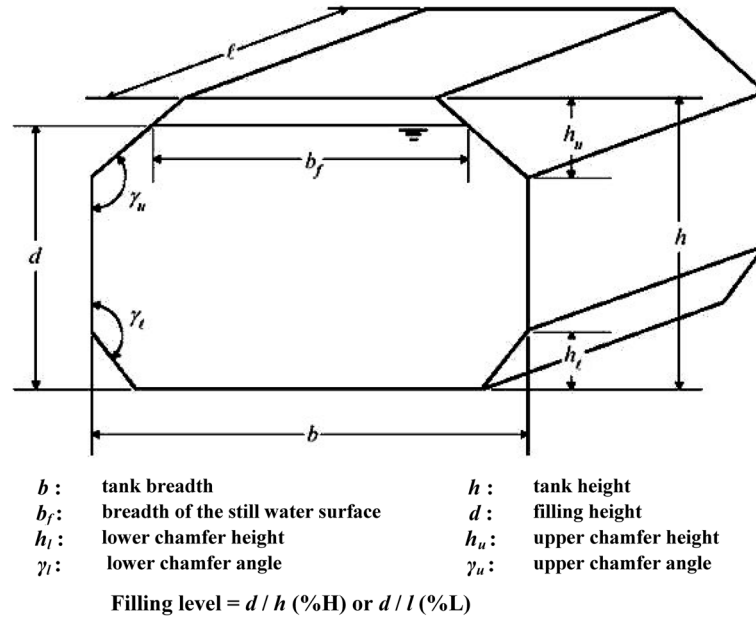


Fig. 1 Membrane-type LNG tank geometry

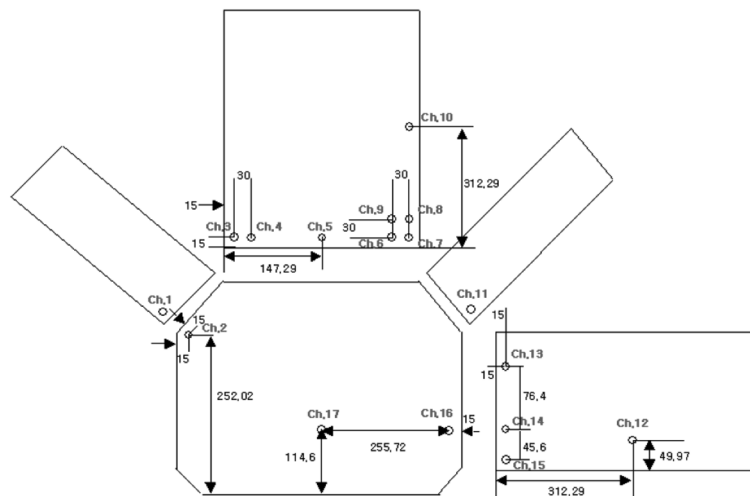


Fig. 2 Location of pressure sensors

In the present study, we consider both the transverse and longitudinal sloshing modes with various combinations of horizontal, vertical and rotational motions. The transverse motion is in the xz -plane while the longitudinal motion is in the yz -plane as shown in Fig. 3. The horizontal direction is along the x -axis for transverse motion, and along y -axis for longitudinal motion. Tables 1 and 2 shows the full scale motion parameters for the three transverse (Cases 1-3) and three longitudinal (Cases 4-6) motion cases considered in the present study. Note that the positive values in Table 2 represent motions from left to right, bottom to top, and counterclockwise rotation.

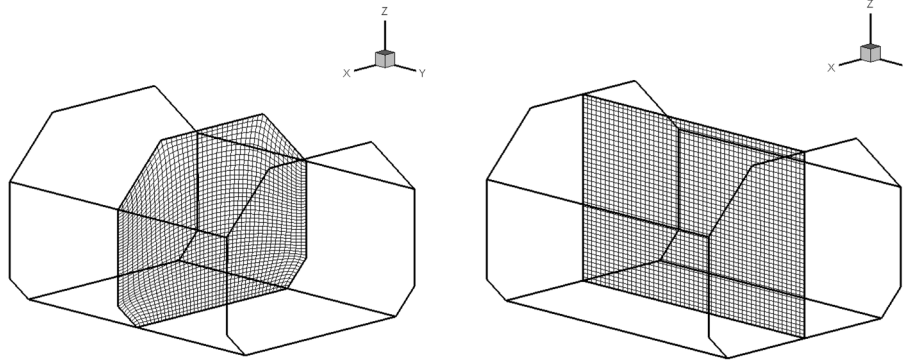


Fig. 3 Two-dimensional numerical grids for transverse and longitudinal motions

Table 1 LNG tank motion periods

Case	Geometry	FLVL(%H)	Compressibility	Direction	Period(s)
1	2D	50%	Incompressible	Transverse	8.98
2	2D	50%	Compressible	Transverse	8.98
3	3D	50%	Compressible	Transverse	8.98
4	2D	92.5%	Incompressible	Longitudinal	9.08
5	2D	92.5%	Compressible	Longitudinal	9.08
6	3D	92.5%	Compressible	Longitudinal	9.08

Table 2 LNG tank motion amplitudes

Case no.	Horizontal motion		Vertical motion		Rotational motion	
	Amplitude (m)	Phase (rad)	Amplitude (m)	Phase (rad)	Amplitude (rad)	Phase (rad)
1 – 3	3.38E+00	-2.14E-01	5.89E+00	3.07E-01	2.48E-03	0.00E+00
4 – 6	1.81E-01	-1.26E+00	6.80E+00	-4.95E-01	9.52E-02	0.00E+00

A 1/70 scale model tank was used in the experiments. The tank motion parameters were scaled down based on the Froude scaling law, while the measured impact pressures were scaled up based on the Euler scaling law, which is consistent with the Froude scaling law. The characteristic time is defined as $T_o = \sqrt{L/g}$ and the pressure is normalized by $P_o = \rho g L$, where L is the characteristic length, g is the gravitational acceleration, and ρ is the density of the fluid. Therefore, the horizontal and vertical motion amplitudes in model scale are 1/70 of the corresponding full scale values, while the motion period is scaled down by $\sqrt{1/70}$. The measured impact pressures reported in the experimental study were scaled up by 70 times.

5. Results and discussions

Numerical simulations were performed using the level-set FANS code for the six cases listed in

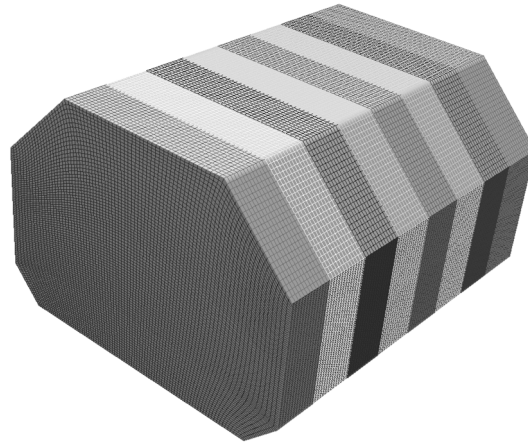


Fig. 4 Numerical grid for three-dimensional simulations

Tables 1 and 2. As noted earlier, the air was treated as compressible and the water was assumed to be incompressible. The surface tension was ignored in the present simulations. In the following, we will present both the 2D and 3D simulation results to illustrate the general performance of the present numerical method.

Both 2D and 3D simulations were performed at full-scale using a constant time increment of $0.001T$ (1,000 time steps per period) to provide accurate resolution of the peak impact pressures. For two-dimensional simulations, a one-block grid with $85 \times 3 \times 85$ nodes was used for the transverse motion cases (Cases 1-3), while a $3 \times 106 \times 85$ rectangular grid was used for longitudinal motion cases (Cases 4-6) as shown earlier in Fig. 3. The three-dimensional grid has $85 \times 106 \times 85$ nodes as shown in Fig. 4. It was partitioned into 8 computational blocks with $85 \times 15 \times 85$ nodes in each block and distributed to 8 processors in order to reduce the turnaround time for 3D simulations. Both the two- and three-dimensional simulations were performed for 20 periods and the wall pressures at selected sensor locations were recorded every time step to facilitate a direct comparison with the experimental data of Lee *et al.* (2006b). The 3D velocity and pressure fields for the entire tank were also saved every 50 time steps to provide more detailed descriptions of the complex three-dimensional flow induced by the sloshing tank. The total CPU time for 20 periods (20,000 time steps) is about 28 hours on a Linux cluster when using 8 processors. The 2D simulations took about 5 hours using a single processor on the same cluster.

A detailed examination of the 3D simulation results indicated that the sloshing flow is highly three-dimensional even though the prescribed transverse or longitudinal motions are strictly two-dimensional. Due to the three-dimensional instability, the impact pressures at the mirror image locations on opposite walls were found to be drastically different under certain flow conditions. In order to provide a more complete understanding of the violent three-dimensional free surface flows, the impact pressure histories were recorded at 48 different locations as shown in Fig. 5. These 48 sensor locations include not only the original 17 pressure sensors in the model tank, but also their mirror images in both x and y directions. This enables us to capture the most critical impact pressures which may occur on the opposite walls of any given pressure sensor locations in the LNG tank. It should be remarked also that the impact pressure on tank walls is highly localized with significant variations between two adjacent grid points. Therefore, the highest impact pressure may

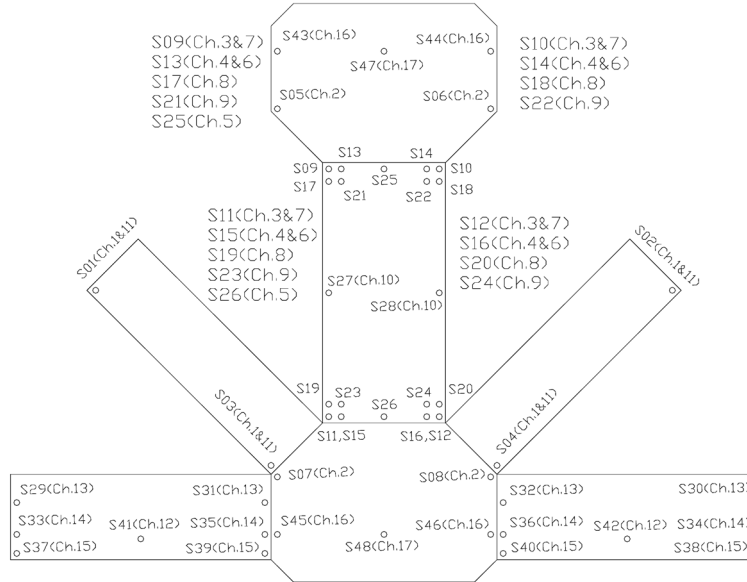


Fig. 5 Grid and sensor locations for three-dimensional simulations

not occur precisely at the sensor locations unless long-duration simulations are performed for several thousand periods to capture the true peak pressure. In view of this, we also save the surface pressure at every computational node on the tank walls over the entire duration (20,000 time steps) of the simulations. This enables us to post-process the wall pressure data to determine the maximum impact pressure in the vicinity of each pressure sensor.

5.1 Cases 1-3: transverse motion at 50% filling level

Fig. 6 shows the trajectory of the LNG tank center for Cases 1 – 3 in prescribed transverse motion. The tank motion was initiated on the upper half of the motion trajectory. A modulation function was applied for the first period of the simulation to prevent excessive fluid motion due to impulsive start. Simulations were performed for 20 periods with a time increment of 0.001T. The wall pressures at 48 sensor locations were recorded every time step, while the 2D and 3D velocity and pressure fields for the entire tank were saved every 50 time steps.

Fig. 7 shows the 2D simulation results of impact pressures for incompressible flow at pressure sensor locations S1 (left) and S2 (right) corresponding to Ch. 11 and its mirror image. Note that Ch. 11 is located on the inclined surface slightly above the lower knuckle point of the upper chamber as shown in Fig. 2. Under the asymmetric transverse tank motion, the pressure patterns are shifted by half-period between the left and right sensors. Furthermore, the peak impact pressures are somewhat higher at the left sensor location S1 because the LNG tank is undergoing a skewed clockwise motion as shown in Fig. 6 which tends to push the fluid towards the upper-left corner. For completeness, the impact pressure histories for 2D compressible flow simulation are also shown in Fig. 8 at the same pressure sensor locations S1 and S2. It is seen that the impact pressures obtained from the compressible flow simulations are significantly higher and more chaotic in comparison with the incompressible flow case. Also, the peak impact pressures at the right sensor location S1

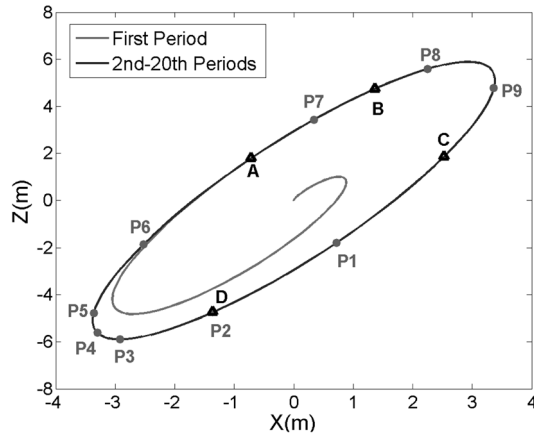


Fig. 6 Tank motion trajectory (distorted scale), Cases 1 – 3

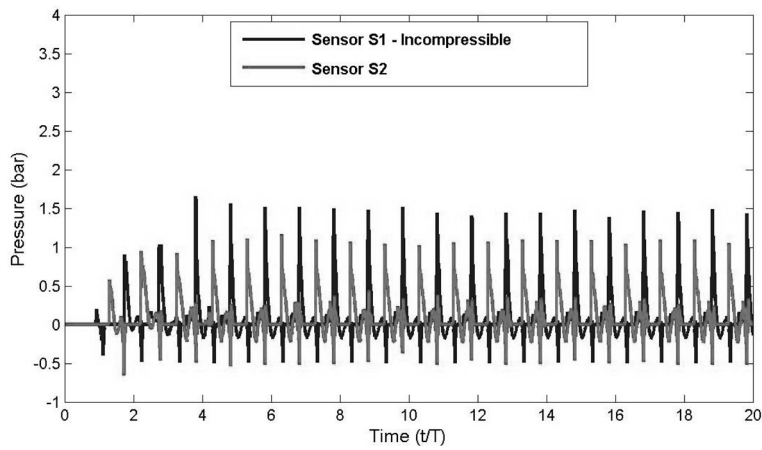


Fig. 7 Impact pressure histories at Ch. 11 for 2D incompressible flow simulations, Case 1

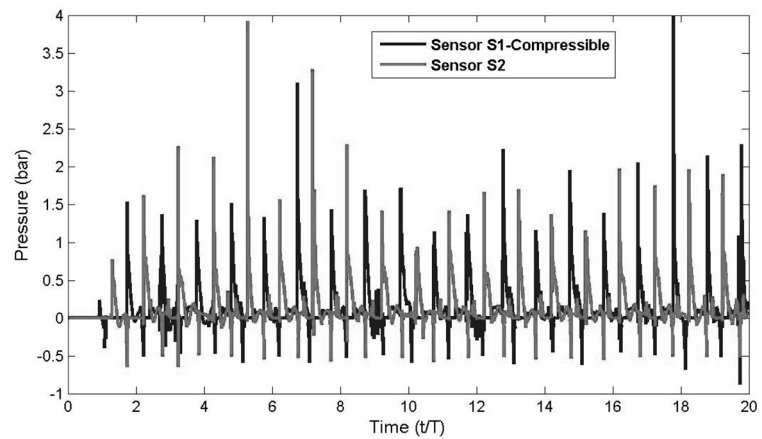


Fig. 8 Impact pressure histories at Ch. 11 for 2D compressible flow simulations, Case 2

were found to be higher than the corresponding peak values at the left sensor location at several time instants. For simplicity, the impact pressures at sensor location S1 will be used in the following comparisons with the experimental data at Ch. 11.

Fig. 9 shows comparisons of the predicted and measured impact pressures at Ch. 11 for the incompressible as well as compressible 2D flows. It is clearly seen that the impact pressure is nearly periodic for the incompressible flow simulation. However, the peak impact pressure is significantly underpredicted for the incompressible flow case. On the other hand, the 2D compressible flow simulation result is much more chaotic and the peak impact pressures are significantly higher than those observed for the incompressible flow case. The peak pressures predicted by the compressible flow model vary between 1.5 and 4.7 bars while the measure peak pressures are in the range of 2.1 and 4.1 bars. In general, the predicted peak pressure is lower than the corresponding measurements but the highest impact pressure is in close agreement with the data.

In order to facilitate a more detailed understanding of the observed impact pressure patterns for incompressible and compressible 2D flows, it is desirable to examine the velocity and density fields induced by the sloshing tank motions as shown in Fig. 10. For the incompressible flow simulation, the non-dimensional density remains constant with $\rho_a / \rho_w = 0.001226$. On the other hand, the air density is determined from the ideal gas law in the compressible flow simulations. For the isothermal condition considered here, the absolute pressure of the compressible air flow is linearly proportional to the air density. In general, the sloshing motion of the water flow tends to increase the air pressure and density under compressible flow conditions. The compressibility effect is most significant when the air is entrapped with the formation of air bubbles as shown in Phases B. It is also interesting to note that the free surface motion is considerably more violent and chaotic under the compressible flow conditions. This chaotic free surface motion has resulted in large variations of peak impact pressures as shown earlier in Figs. 8 and 9.

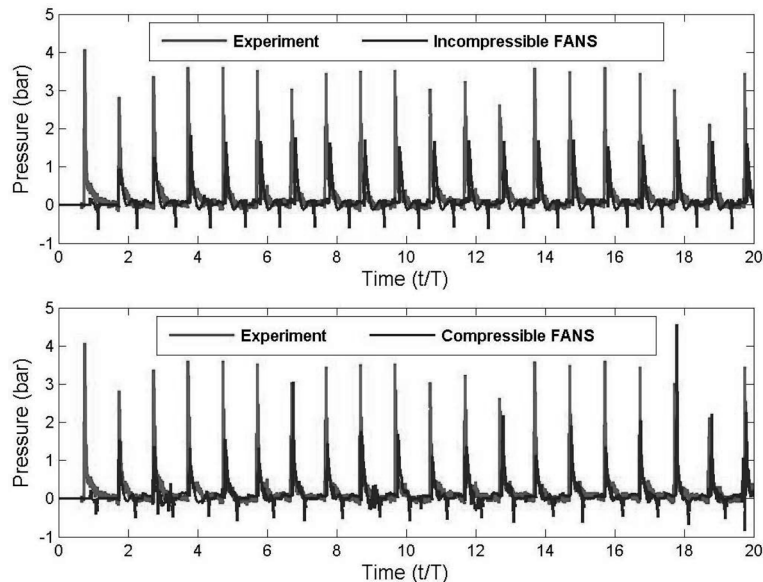


Fig. 9 Comparisons of measured and predicted impact pressure histories at Ch. 11 for incompressible and compressible flow models

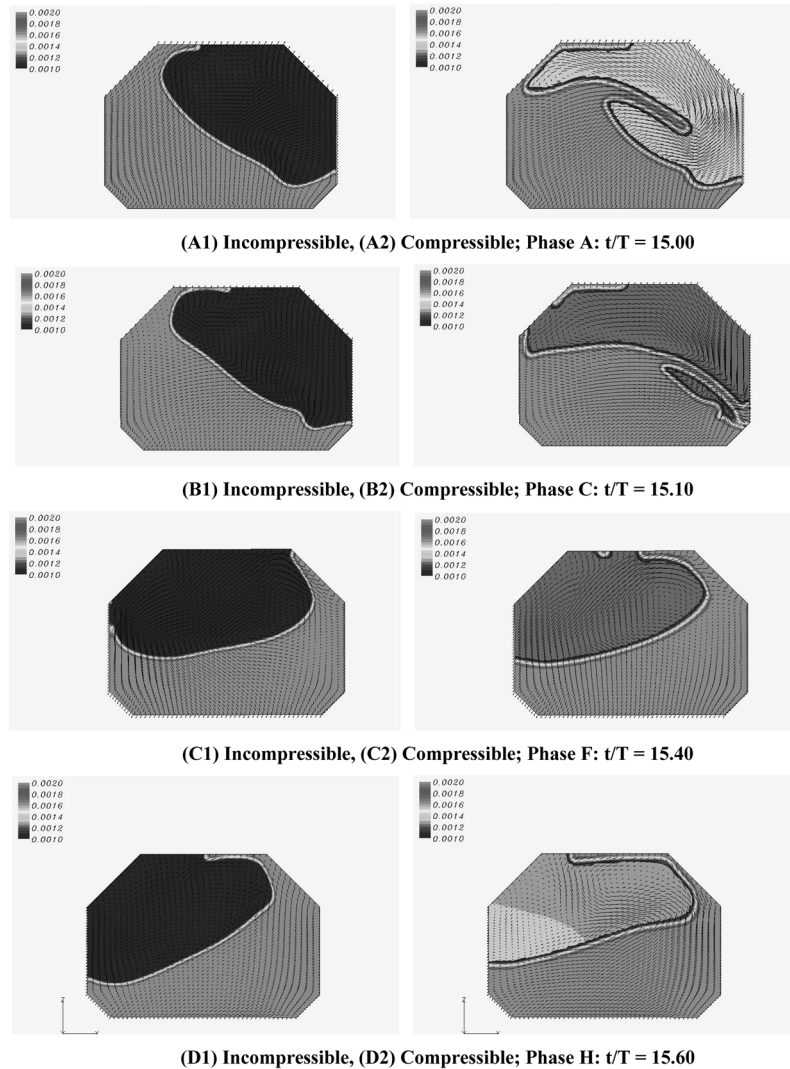


Fig. 10 2D free surface patterns, velocity vectors and density contours, Cases 1 and 2

Fig. 11 shows a detailed comparison of the measured and predicted time histories of the tank wall pressures at sensor location S1 over one harmonic excitation period between $t/T = 6.4$ and 7.4 . It should be noted that the peak impact for compressible flow simulations occurs at $t/T = 6.747$ when the tank reaches the lower-left corner (i.e., Phase P4) of the motion trajectory shown in Fig. 6. On the other hand, the peak impact for the incompressible flow case occurs at a later time $t/T = 6.827$ between Phases P5 ($t/T = 6.80$) and P6 ($t/T = 6.90$) in Fig. 6. For convenience, different phase shifts were applied to the experimental data to match instants of peak impact pressures for both the incompressible and compressible cases. It is seen that the impact pressure history obtained from the compressible flow model is in very good agreement with the corresponding measurements.

For completeness, the pressure contours at 9 selected phases (P1-P9 in Fig. 6) are also shown in Fig. 12 to facilitate a more detailed understanding of the sloshing impact pressure patterns for the

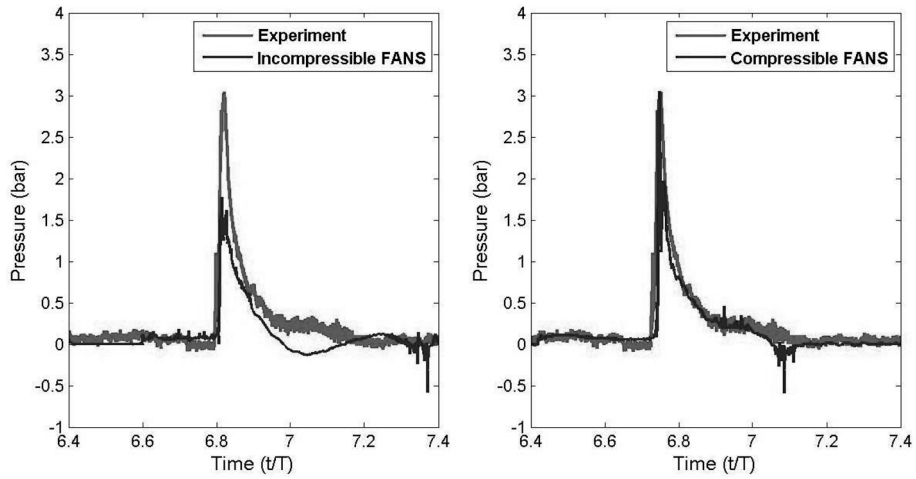


Fig. 11 Comparisons of measured and predicted impact pressure histories, Cases 1 and 2

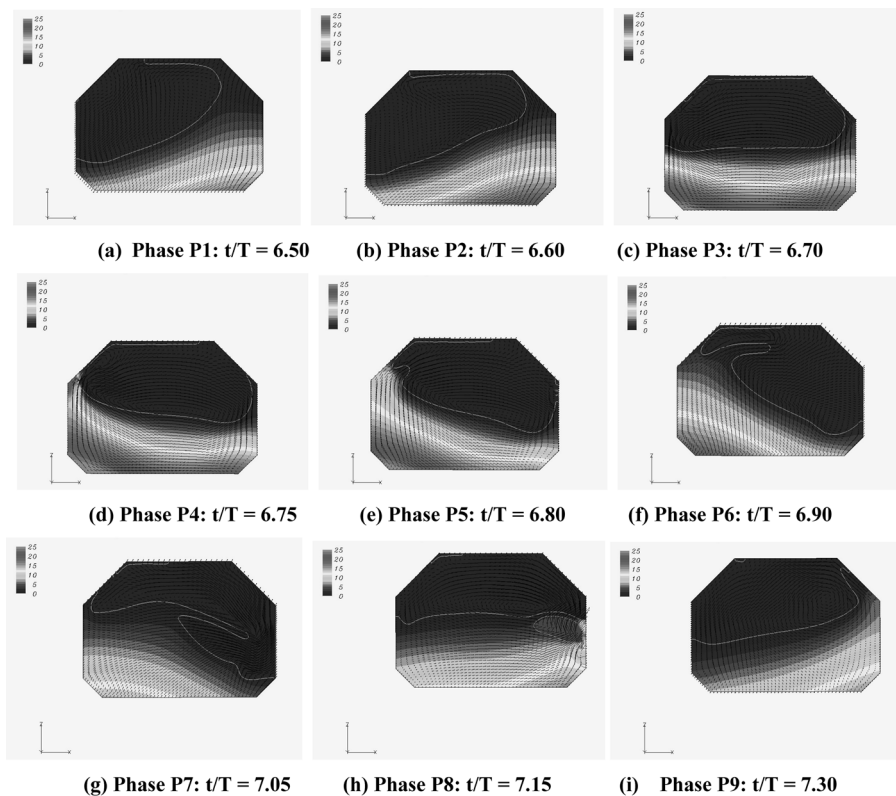


Fig. 12 Pressure contours and velocity vector plots, Case 2

compressible flow case. At $t/T = 6.5$ (Phase P1), the tank is descending towards the lower-left corner while the fluid is pushed towards the upper-right corner. As the LNG tank continues to move downward between $t/T = 6.5$ and 6.75 (Phase P4), the sloshing water is pushed from the upper-right to the lower-

left corner due to rapid deceleration of the LNG tank. At $t/T = 6.75$, the tank reaches the lower-left corner and begins to ascent along the upper half of the elliptic motion trajectory. Due to the change of motion direction, the sloshing water is moving towards the left wall and exerts a large pressure force on the tank bottom as shown in Phases P3-P5 of Fig. 12. At $t/T = 6.7$, the inclined wall of the upper chamfer was completely dry with negligible air pressure as shown earlier in Fig. 11. The peak impact occurs at $t/T = 6.747$ when the pressure sensor S1 was suddenly inundated by the rapidly rising water on the left wall. After the initial impact, the water continues to move upward and hit the tank top while the pressure at sensor location S1 returns gradually to zero between $t/T = 6.8$ and 7.1 (i.e., Phases P5-P8).

As the water was pushed upward along the left wall towards the tank top wall, a portion of the sloshing flow was detached from the inclined surface of the upper chamfer under the effect of gravity to form a splashing water jet as shown in Phases P5-P9. Shortly before $t/T = 7.15$, the water jet hit the tank wall and produced a small air bubble adjacent to the right side wall. The pressure of the entrapped air is somewhat higher than the open air flow in the upper tank. This resulted in an increase of density inside the air bubble as noted earlier in Fig. 10. It is clearly seen that the splashing jet produced highly localized impacts with sharp increase of impact pressures at the points of contact with the right side wall.

In addition to the 2D incompressible and compressible flow simulations, calculations were also performed for 3D compressible flow to investigate the three-dimensional effect of the violent free surface in the sloshing LNG tank. Figs. 13 and 14 show the predicted three-dimensional sloshing

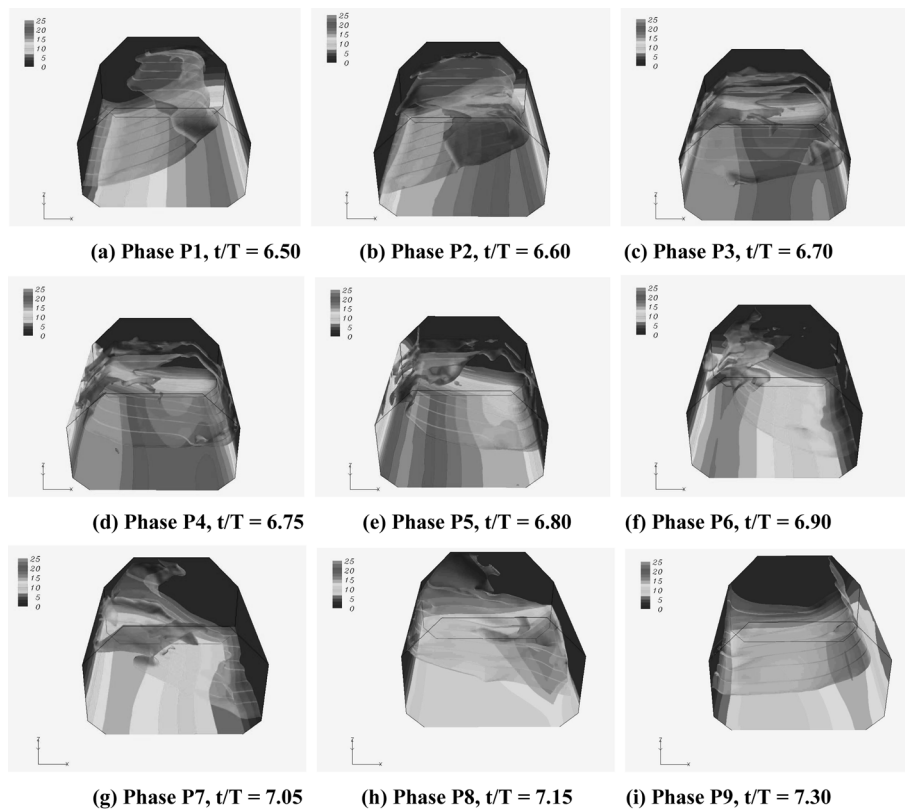


Fig. 13 Free surface patterns and wall pressure contours between $t/T = 6.50$ and 7.30, Case 3

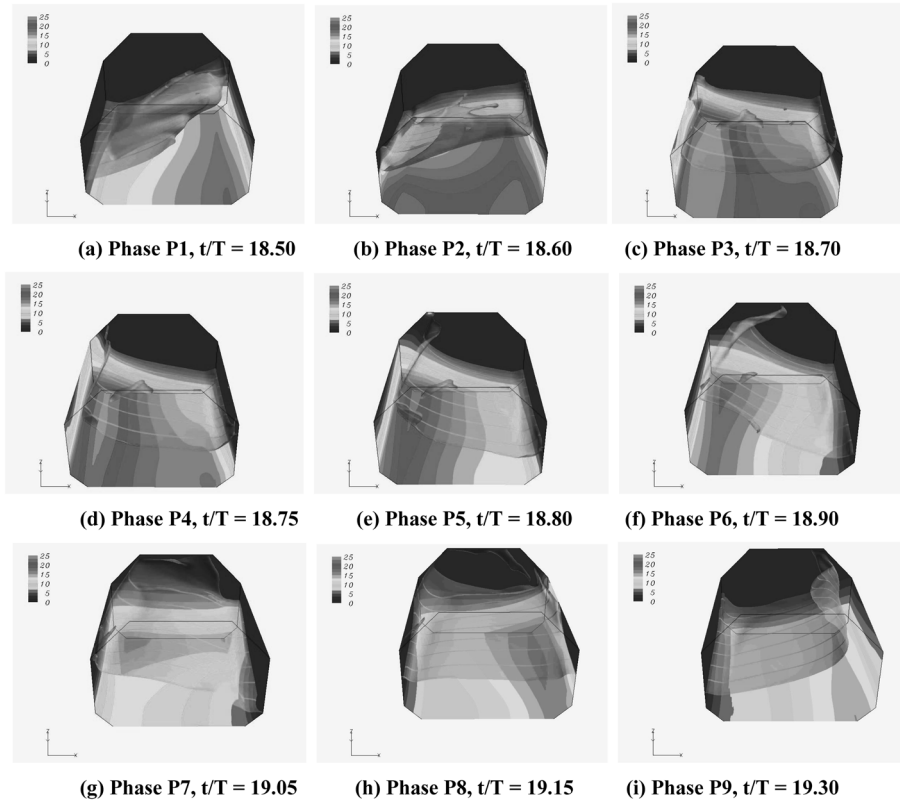


Fig. 14 Free surface patterns and wall pressure contours between $t/T = 18.50$ and 19.30 , Case 3

flow patterns and pressure contours on the tank walls at 18 time instants which correspond to the same Phases P1-P9 in Fig. 6 but are 12 excitation periods apart. During the initial stage of the harmonic excitation motion, the sloshing flow patterns are weakly three-dimensional as shown in Fig. 13 at $t/T = 6.5\sim 7.3$. As the simulation proceeded for longer duration, the sloshing flow becomes increasingly chaotic and strongly three-dimensional. More specifically, a swirling motion was observed in Fig. 14 at $t/T = 18.5\sim 19.3$. Similar swirling flow patterns were also observed in the experiment under the same tank excitation condition. Similar to the 2D simulations which show the presence of entrapped air in closed bubbles, the 3D results also predicted the presence of air pockets at several tank cross sections (i.e., 2D slices at constant- y planes). However, those 2D air pockets do not form closed air bubbles and the air in the pocket is able to escape in the longitudinal direction of the tank. Consequently, the compressibility effects associated with the air trapping is less important for the 3D cases.

As a result of the 3D swirling flow pattern, the impact pressures at mirror-image sensor locations (S1, S3) and (S2, S4) shown in Fig. 15 becomes asymmetric at large t/T even though the excitation motion is strictly two-dimensional. A close examination of the impact pressure histories at all 4 sensor locations indicates that the largest impact tends to occur at sensor S3. Therefore, the pressure histories at sensor location S3 will be used in the following comparisons with 2D simulation result and experimental data as shown in Fig. 16. In general, the 3D pressures at sensor location S3 are in close agreement with the corresponding 2D results but the peak impact pressures are somewhat

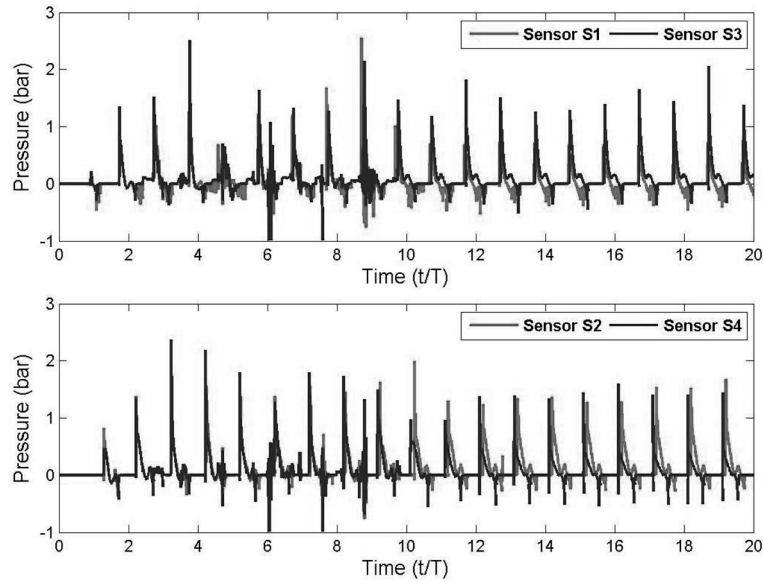


Fig. 15 Impact pressure histories in 3D tank at sensor locations S1, S2, S3, S4, Case 3

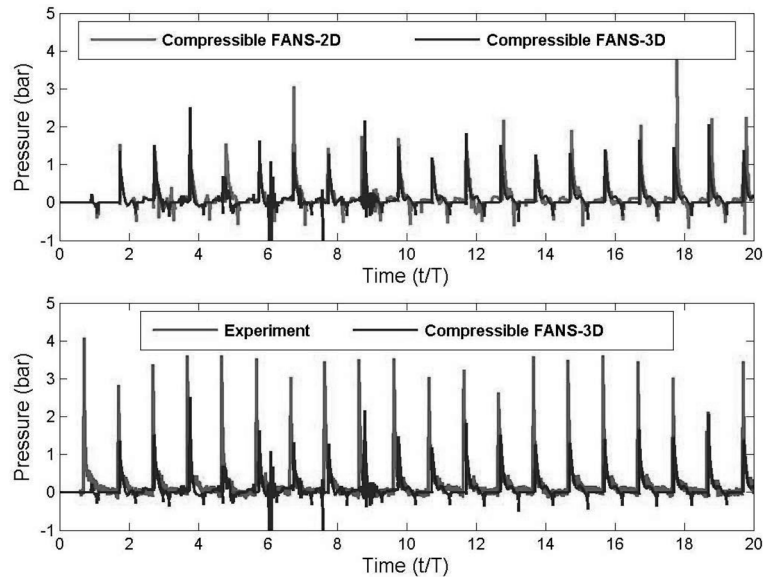


Fig. 16 Comparisons of 3D impact pressures with 2D simulations and experiment for transverse motion cases

lower at large t/T . This can be attributed to the three-dimensional flow pattern which produced a more chaotic and highly localized impact on the tank walls. Since the impact pressure is highly localized and varies from one sloshing period to another, it is difficult to capture the true maximum impact pressure unless the numerical simulations were performed for a much longer duration with thousands of sloshing periods. For short duration simulations, it is desirable to record the maximum impact pressure over the entire tank wall since the peak impact pressure may not occur precisely at

any specific sensor locations. It should also be remarked that the three-dimensional sloshing motion tends to reduce the risk of tank damage since the maximum impact force is less likely to occur at the same location when comparing with purely two-dimensional simulations.

5.2 Cases 4 – 6: longitudinal motion at 92.5% filling level

Fig. 17 shows the longitudinal motion trajectory (in yz -plane) of the LNG tank for Cases 4-6 with a 92.5% filling level. It should be noted that the horizontal motion amplitude is only 0.181 m while the vertical motion is much larger with a heave amplitude of 6.80 m. In addition to the large amplitude vertical motion, the tank also experienced a fairly large amplitude pitch motion with a maximum pitch angle of $\pm 5.45^\circ$. A modulation function was again applied for the first cycle of harmonic excitation to eliminate the pressure oscillations caused by the impulsive start of the LNG tank motion. Both the 2D and 3D simulations were performed for 20 periods, and the wall pressures at selected sensor locations were recorded every time step to facilitate a direct comparison with the experimental data. At the 92.5% filling level, the free surface motion and high impact pressure regions are confined to the upper chamfer near the tank top. In view of this, the numerical grid was redistributed in the vertical direction to provide more accurate resolution of the impact pressures in the upper chamfer.

Fig. 18(a) shows the 2D compressible flow simulation results of impact pressures for the left (S25) and right (S26) pressure sensors corresponding to Ch. 3 on the top wall. Due to the asymmetric tank motion, the impact pressure histories and the peak impact pressures are somewhat different at sensor locations S25 and S26. However, the differences in peak impact pressures are not large since the sloshing flow is dominated by the large amplitude heave motion with negligible horizontal displacements. For completeness, comparisons were also made in Fig. 18(b) between the compressible and incompressible simulation results at sensor location S25 to evaluate the effect of compressibility. In general, the impact pressures predicted by the compressible flow model are more chaotic and the maximum impact pressure is about 25% higher than the corresponding peak impact pressure for the incompressible flow.

Fig. 19 shows the time histories of the measured and predicted pressures at Ch. 3 on the top

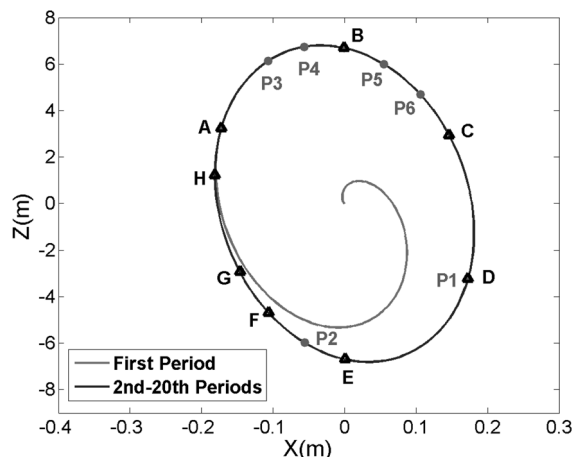


Fig. 17 Tank motion trajectory (distorted scale), Cases 4 – 6

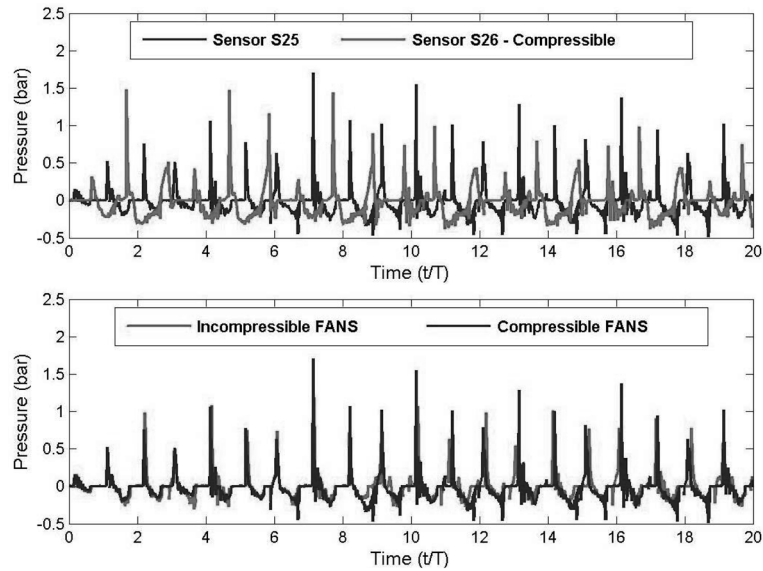


Fig. 18 2D pressure histories at Ch. 3, Case 4 – 5

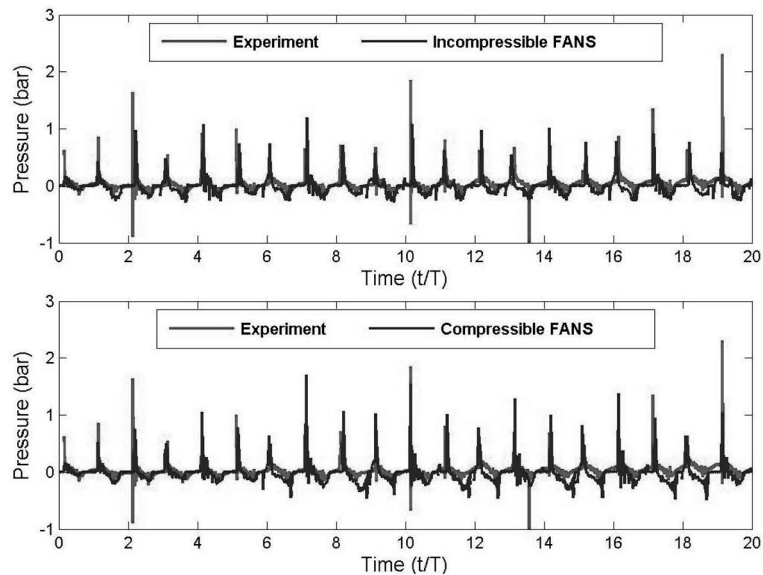


Fig. 19 Comparisons of measured and predicted impact pressures at Ch. 3, Cases 4 – 5

surface of the LNG tank for both the 2D incompressible and compressible flow models. Note that Ch.3 and Ch.7 are mirror images on opposite side of the tank top wall as shown in Fig. 2. In general, the compressible flow simulation results are in somewhat better agreement with the corresponding measurements. It is seen that the peak impact pressure on the top wall is relatively low for this high filling case since the free surface motion is less violent in the confined ullage space. Furthermore, both the measured and predicted pressure histories at Ch. 3 show the presence of negative pressures (i.e., below atmospheric pressure) between two adjacent peak impacts. A

detailed examination of the simulation results indicates that the partial vacuum was caused by the sloshing water receding from the top wall following each impact.

Fig. 20 shows the predicted density contours and velocity vectors in the LNG tank at 4 different time instants $t/T = 17.00, 17.35, 17.70,$ and 17.80 . The incompressible flow results are shown in the left column with constant air density of $\rho_a / \rho_w = 0.001226$. For the compressible flow results in the right column, the air density is linearly proportional to the absolute air pressure following the ideal

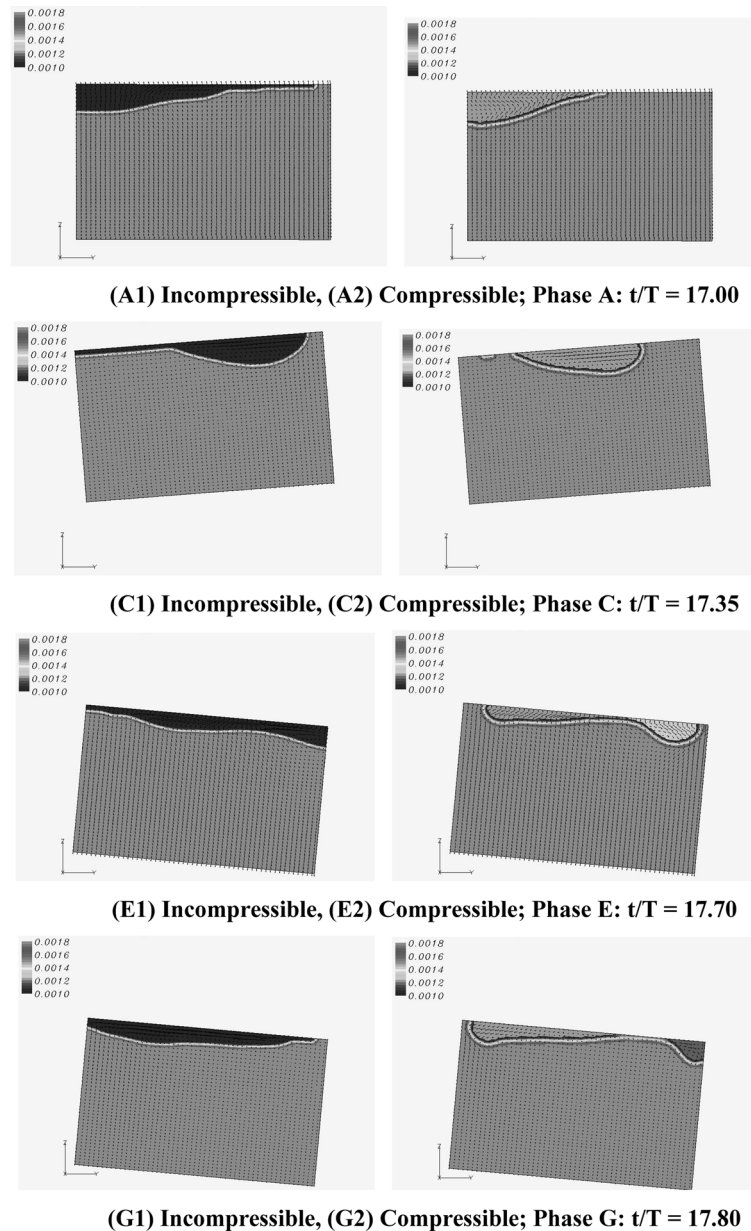


Fig. 20 2D free surface patterns, velocity vectors and density contours, Cases 4 and 5

gas law. Similar to those observed earlier for the transverse motion cases, the sloshing water flow tends to increase the air pressure and density under compressible flow conditions. The compressibility effect is most significant when the air is entrapped in the upper-right corner as shown in Phases E and G. It is quite clear that the free surface patterns are more complex and chaotic under compressible flow conditions.

Fig. 21 shows a detailed comparison of the measured and predicted time histories of the tank wall pressures at sensor location S25 between $t/T = 10.1$ and 10.5 . A detailed examination of the impact pressure histories indicates that the peak impact for compressible flow occurred at $t/T = 10.144$, while the peak impact for incompressible flow was observed somewhat later at $t/T = 10.201$. For convenience, different phase shifts were applied to the experimental data to facilitate the comparison of peak impact pressures. It is seen that the incompressible flow model failed to capture the high frequency pressure oscillations observed in the measurement. On the other hand, the compressible flow simulation results clearly exhibit a low frequency pressure oscillation. It should be noted that the present simulations were performed using a time increment of $\Delta t/T = 0.001$ (i.e., 1000 time steps per period) while the sampling rate for the experiment is about 21700 per period. A much finer time step size is needed in order to capture the high-frequency oscillations observed in the experiments. Nevertheless, the present study clearly demonstrated the feasibility of resolving impact pressure oscillations using a compressible flow model.

For completeness, the pressure contours at 8 selected phases (P1-P8 in Fig. 17) are also shown in Fig. 22 to facilitate a more detailed understanding of the sloshing impact pressure patterns for the high filling level case considered here. Between $t/T = 9.5$ (Phase P1) and $t/T = 9.75$, the tank past the lower-right corner and began to ascend towards the upper-left corner. The wall pressure at the tank bottom reaches maximum around the lower-right corner of the motion trajectory since the hydrodynamic pressure due to fluid momentum acts in the same direction as the hydrostatic pressure force during the tank descend. As the tank moves towards the top-left corner, the pressure on the bottom wall reduces rapidly since the hydrodynamic pressure acts in the opposite direction of the gravity. When the tank reached the top-right position and began to descend, the sloshing fluid

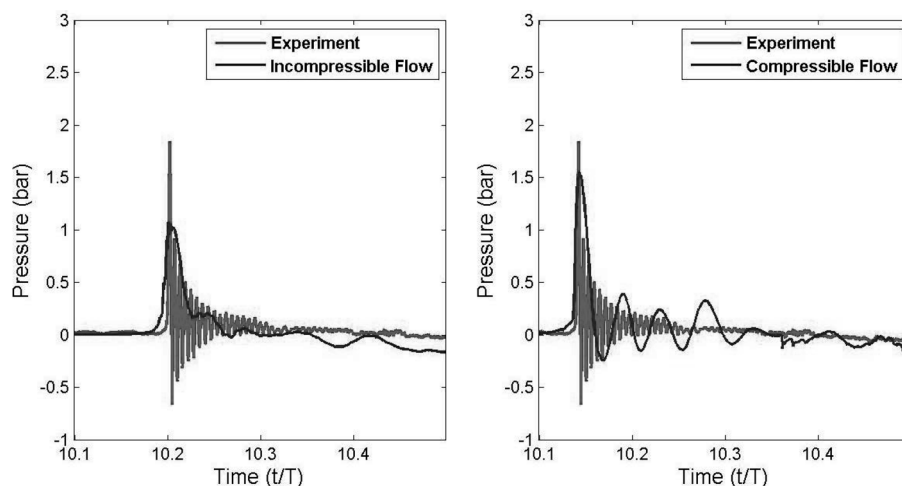


Fig. 21 Comparisons of measured and predicted impact pressure histories between $t/T = 10.1 - 10.5$, Cases 4 and 5

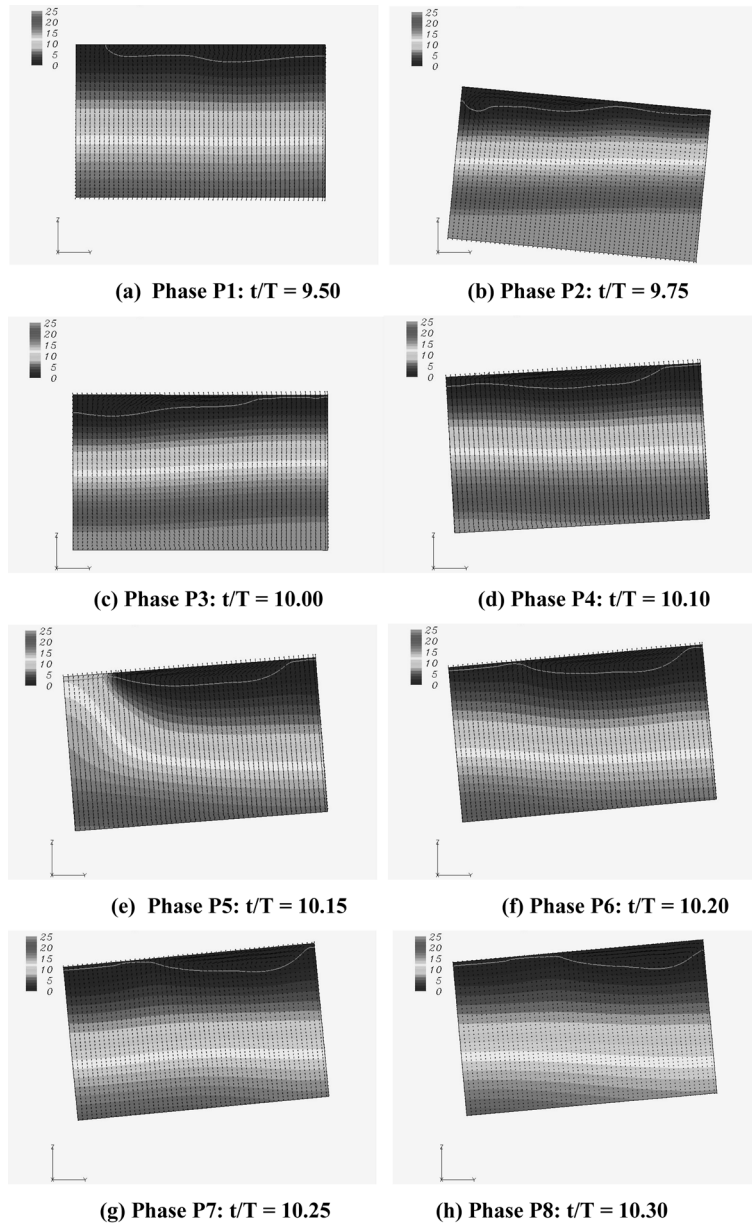


Fig. 22 Pressure contours and velocity vector plots, Case 5

continued to move upward and exerted a large hydrodynamic pressure on the top wall of the LNG tank as shown in Phase P5 ($t/T = 10.150$). As noted earlier, the peak impact pressure was observed at $t/T = 10.144$ just before the tank reached the top of the motion trajectory. After the peak impact, a thin layer of air was observed near the upper-left corner of the tank where the pressure sensor S25 is located. A detailed examination of the simulation results indicate that the pressure oscillations shown in Fig. 21 were associated with the compressibility effects in the thin air gap.

In addition to the 2D simulations, calculations were also performed for 3D compressible flow to

investigate the three-dimensional effect in the upper chamfer under the high filling level condition. Fig. 23 shows the three-dimensional sloshing flow patterns and wall pressure contours at 8 phases A-H in the motion trajectory plot (Fig. 17). It is quite clear that the free surface elevations are somewhat higher along the inclined wall due to the narrowing of the cross sectional area near the tank top. Furthermore, the flow is strongly three-dimensional even though the tank excitation motion is strictly two-dimensional. A detailed examination of the animation movies clearly shows the formation of closed air bubbles between $t/T = 17.45$ and 17.70 (see Phases D and E) on the left

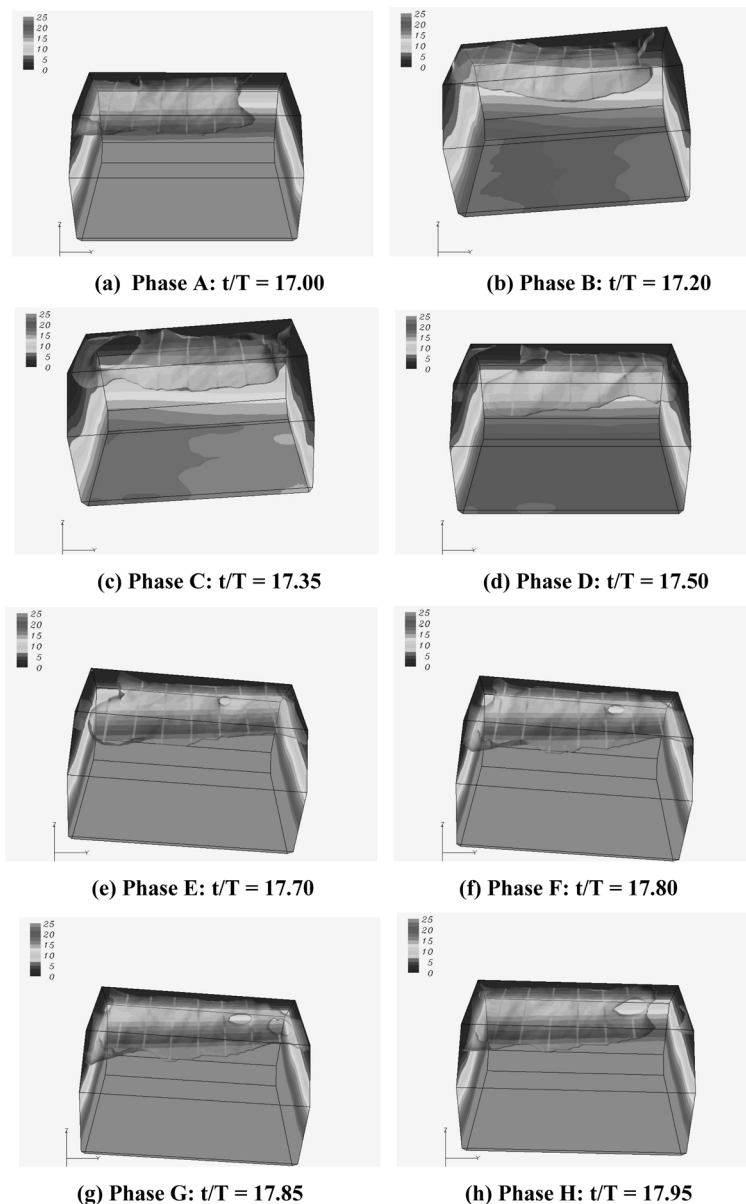


Fig. 23 Free surface patterns and wall pressure contours, Case 6

corner of the upper chamfer. It is also observed that the free surface motion for Case 6 is less violent and the impact pressures are significantly lower than those observed earlier for the lower filling level cases (i.e., Case 3).

Fig. 24 shows the impact pressure histories at sensor locations S09, S10, S11 and S12 corresponding to Ch. 3 and its mirror-image locations. It is seen that the sloshing flow is highly three-dimensional with large differences in impact pressures at four corners of the top wall. In general, the impact pressure history at sensor location S09 is in closer agreement with the 2D experimental data. Therefore, we shall use the simulation results at sensor S09 in the following comparisons. Note that sensor S25 used in earlier two-dimensional simulations is located at the middle point between the sensors S09 and S10, so the impact pressures at S09 is in phase with that at S25. Similarly, the 3D impact pressure histories at S11 and S12 are in phase with the 2D impact pressures at sensor location S26.

Fig. 25 shows a comparison of the impact pressure history at sensor location S09 with the experimental data at Ch. 3 and the 2D results at sensor location S25. In general, the 3D peak impact pressures are somewhat lower than the corresponding 2D simulation results. As noted earlier, the three-dimensional sloshing flow produced highly localized impact which may not occur precisely at the sensor locations for short duration simulations. Nevertheless, the general impact pressure patterns are still in reasonable agreement with the corresponding measurements. It should also be noted that both measurements and simulations show that the sloshing impact is highly chaotic with both single-peak and oscillatory pressure patterns occur at the same sensor location as seen in Fig. 26 for two different impact events between $t/T = 3 - 3.5$ and $t/T = 6 - 6.5$. Due to the chaotic nature of the sloshing impact, it is anticipated that much longer simulations over many more excitation periods are needed in order to accurately predict the maximum impact pressure. However, the short-duration simulations performed in the present study still provide very useful information on the sloshing flow patterns as well as detailed impact pressures on all surfaces of the sloshing tank.

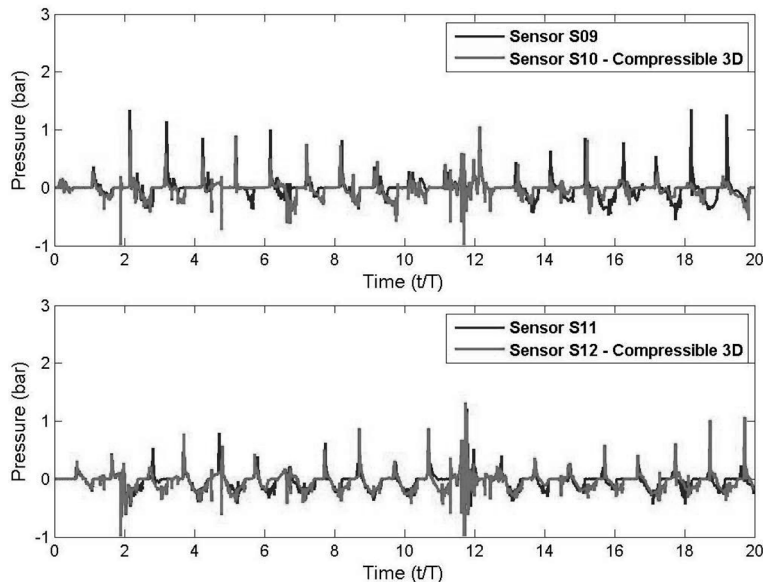


Fig. 24 Impact pressure histories at sensor locations S09, S10, S11 and S12, Case 6

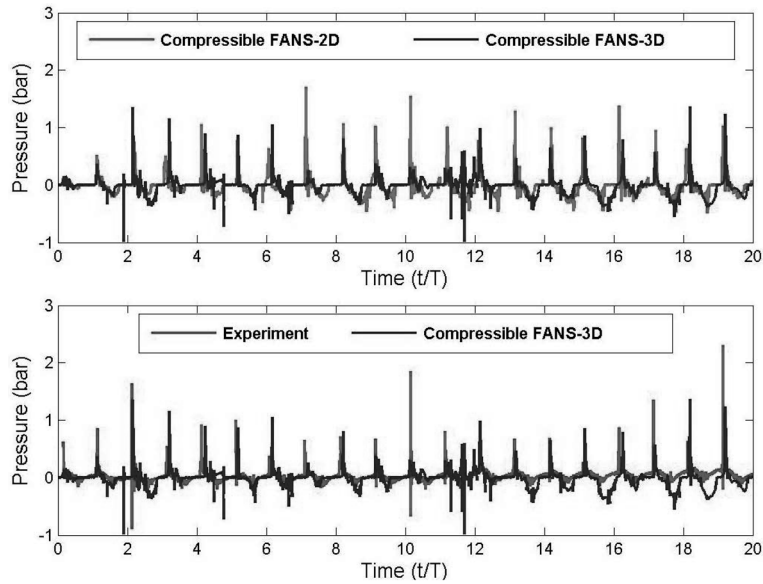


Fig. 25 Comparisons of 3D impact pressures with 2D simulations and experiment for longitudinal motion cases

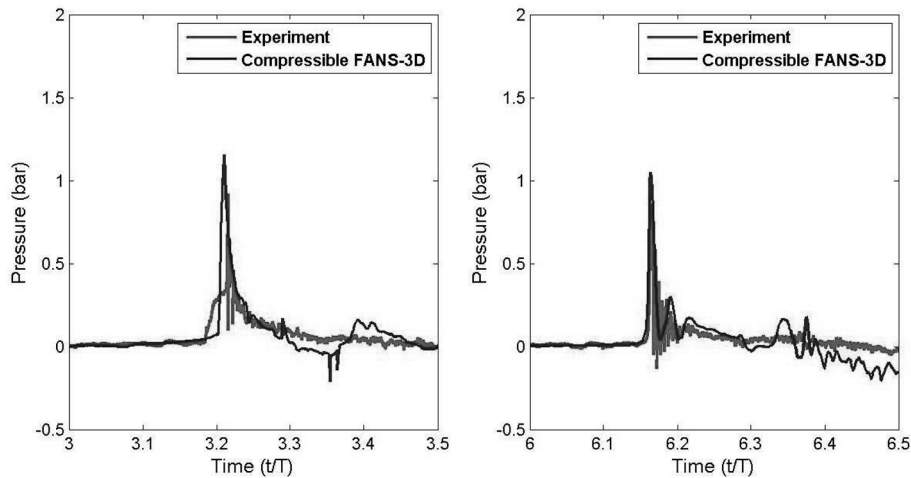


Fig. 26 Comparisons of measured and predicted impact pressures, Case 6

6. Conclusions

In the present study, violent sloshing flows induced by the transverse and longitudinal motions of a membrane-type LNG tank were solved using the level-set Finite-Analytic Navier-Stokes (FANS) method. Calculations were performed for both the 2D and 3D LNG tanks using compressible and incompressible flow models. Three-dimensional instabilities of sloshing flow were observed for both the transverse and longitudinal motion cases and confirmed by the experiments even though the tank excitation forces are strictly two-dimensional. In general, the compressible flow model produced more chaotic sloshing flow patterns and higher impact pressures. Moreover, the high-

frequency pressure oscillations observed in the experiment for high filling level cases were successfully captured in the compressible flow model. The predicted impact pressures for both the transverse and longitudinal motion cases are in good agreement with the corresponding experimental data although the peak pressures are somewhat underpredicted and the high-frequency pressure oscillations were under-resolved.

References

- Cao, Y., Graczyk, M., Pakozdi, C., Lu, H., Huang, F. and Yang, C. (2010), "Sloshing load due to liquid motion in a tank, comparison of potential flows, CFD, and experiment solutions," *Proceedings of the 20th International Offshore and Polar Engineering Conference*, Beijing, China.
- Chen, H.C. (2010), "Time-domain simulation of nonlinear wave impact loads on fixed offshore platform and decks", *Int. J. Offshore Polar*, **20**(4), 275-283.
- Chen, H.C. and Chen, M. (1998), "Chimera RANS Simulation of a berthing DDG-51 ship in translational and rotational motions", *Int. J. of Offshore Polar*, **8**(3), 182-191.
- Chen, H.C., Patel, V.C. and Ju, S. (1990), "Solutions of Reynolds-averaged Navier-Stokes equations for three-dimensional incompressible flows", *J. Comput. Phys.*, **88**(2), 305-335.
- Chen, H.C. and Yu, K. (2006), "Numerical simulation of wave runup and greenwater on offshore structures by a level-set RANS method," *Proceedings of the 16th International Offshore and Polar Engineering Conference*, San Francisco, California.
- Chen, H.C. and Yu, K. (2009), "CFD simulation of wave-current-body interactions including greenwater and wet deck slamming," *J. Comput. and Fluids*, **38**(5), 970-980.
- Chen, Y.G., Price, W.G. and Temarel, P. (2009), "Numerical simulation of liquid sloshing in LNG tanks using a compressible two-phase flow model", *Proceedings of the 19th International Offshore and Polar Engineering Conference*, Osaka, Japan.
- Faltinsen, O.M., Rognebakke, O.F., Lukovski, I.A. and Timoka, A.N. (2000), "Multidimensional modal analysis of nonlinear sloshing in a rectangular tank with finite water depth", *J. Fluid Mech.*, **407**, 201-234.
- Guilcher, P.M., Oger, G., Brosset, L., Jacquin, E., Grenier, N. and Touze, D.L. (2010), "Simulation of liquid impacts with a two-phase parallel SPH model", *Proceedings of the 20th International Offshore and Polar Engineering Conference*, Beijing, China.
- Hwang, S.H. (2006), "Experimental and numerical investigation on sloshing impact load", Ph.D. Dissertation, Pusan National University, Korea.
- Iglesias, A.S., Rojas, L.P. and Rodriguez, R.Z. (2004), "Simulation of anti-roll tanks and sloshing type problems with smoothed particle hydrodynamics", *Ocean Eng.*, **31**(8-9), 1169-1192.
- Jiang, G.S. and Shu, C.W. (1996), "Efficient implementation of weighted ENO schemes", *J. Comput. Phys.*, **126**, 202-228.
- Jiang, G.S. and Peng, D.P. (2000), "Weight ENO schemes for hamilton-jacobi equations", *SIAM J. Sci. Comput.*, **21**(6), 2126-2143.
- Kim, Y. (2001), "Numerical simulation of sloshing flows with impact load", *Appl. Ocean Res.*, **23**(1), 53-62.
- Kim, Y. (2004), "Numerical study on slosh-induced impact pressures on three-dimensional prismatic tanks", *Appl. Ocean Res.*, **26**(5), 213-216.
- Lee, D.H., Kim, M.H., Kwon, S.H., Kim, J.W. and Lee, Y.B. (2005a), "A parametric sensitivity study on LNG tank sloshing loads by numerical simulations", *Ocean Eng.*, **34**(1), 3-9.
- Lee, J.M., Lee, Y.B., Sim, I.H. and Kim, J.W. (2006a), "Validation and study of SLOFE3D simulation and model test for LNG tank ship 140,000 m³", ABS-DSME JDP, Technical Report TR 2006-01, Houston, Texas, USA.
- Lee, Y.B., Sim, I.H., Kim, Y.S., Jung, J.H., Park, J.S., Kwon, S.H. and Jang, T.S. (2005b), "Experimental study on sloshing for large LNGC design", *Proceedings of the 15th International Offshore and Polar Engineering Conference*, Seoul, Korea.
- Lee, Y.B., Lee, J.M., Kim, Y.S., Jung, J.H., Jung, D.W. and Kwon, S.H. (2006b), "An experimental study of impulsive sloshing load acting on LNGC tank", *Proceedings of the 16th International Offshore and Polar*

- Engineering Conference*, San Francisco, USA.
- Loots, E., Pastoor, W., Buchner, B. and Tveitnes, T. (2004), "The numerical simulation of LNG sloshing with an improved volume of fluid method", *Proceedings of the 23rd International Conference on Offshore Mechanics and Arctic Engineering*, Vancouver, Canada.
- Nam, B.W. and Kim, Y. (2006), "Simulation of two-dimensional sloshing flows by SPH method", *Proceedings of the International Offshore and Polar Engineering Conference*, San Francisco, California, USA.
- Osher, S. and Sethian, J.A. (1988), "Fronts propagating with curvature-dependent speed: algorithms based on Hamilton-Jacobi formulations", *J. Comput. Phys.*, **79**(1), 12-49.
- Peric, M., Zorn, T., Moctar, O., Schellin, T.E. and Kim, Y.S.(2007), "Simulation of sloshing in LNG-tanks", *Proceedings of the 26th International Conference on Offshore Mechanics and Arctic Engineering*, San Diego, California, USA.
- Sethian, J.A. (1996), *Level Set Methods*, Cambridge University Press.
- Sussman, M. and Fatemi, E., (1999). "An efficient, interface-preserving level set redistancing algorithm and Its Application to interfacial incompressible fluid flow", *SIAM J. Sci. Comput.*, **20**, 1165–1191.
- Wemmenhove, R., Luppés, R., Veldman, A.E.P. and Bunnik, T. (2007), "Numerical simulation of sloshing in LNG tanks with a compressible two-phase model", *Proceedings of the 26th International Conference on Offshore Mechanics and Arctic Engineering*, San Diego, California, USA.
- Wemmenhove, R., Iwanowski, B., Lefranc, M., Veldman, A.E.P., Luppés, R. and Bunnik, T. (2009), "Simulation of Sloshing dynamics in a tank by an improved volume-of-fluid method", *Proceedings of the 19th International Offshore and Polar Engineering Conference*, Osaka, Japan.
- Yu, K., Chen, H.C., Kim, J.W. and Lee, Y.B. (2007), "Numerical simulation of two-phase sloshing flow in LNG tank using finite-analytic level-set method", *Proceedings of the 26th International Conference on Offshore Mechanics and Arctic Engineering*, San Diego, California, USA.
- Yue, W.S., Lin, C.L. and Patel, V.C. (2003), "Numerical simulation of unsteady multidimensional free surface motions by level set method", *Int. J. Numer. Meth. Fl.*, **42**(8), 853-884.